Effect of component substitution on the atomic dynamics in glass-forming binary metallic melts

B. Nowak,[1,*] D. Holland-Moritz,[1] F. Yang,[1] Th. Voigtmann,[1,2] Z. Evenson,[3] T. C. Hansen,[4] and A. Meyer[1]

[1]*Institut für Materialphysik im Weltraum, Deutsches Zentrum für Luft- und Raumfahrt (DLR), 51170 Köln, Germany*

[2]*Physik-Department, Heinrich-Heine Universität Düsseldorf, Universitätsstrasse 1, 40225 Düsseldorf, Germany*

[3]*Heinz Maier-Leibnitz Zentrum (MLZ) and Physik Department, Technische Universität München, 85748 Garching, Germany*

[4]*Institut Laue-Langevin (ILL), 71 avenue des Martyrs, 38000 Grenoble, France*

(Received 24 May 2017; revised manuscript received 10 July 2017; published 7 August 2017)

We investigate the substitution of early transition metals (Zr, Hf, and Nb) in Ni-based binary glass-forming metallic melts and the impact on structural and dynamical properties by using a combination of neutron scattering, electrostatic levitation (ESL), and isotopic substitution. The self-diffusion coefficients measured by quasielastic neutron scattering (QENS) identify a sluggish diffusion as well as an increased activation energy by almost a factor of 2 for $Hf_{35}Ni_{65}$ compared to $Zr_{36}Ni_{64}$. This finding can be explained by the locally higher packing density of Hf atoms in $Hf_{35}Ni_{65}$ compared to Zr atoms in $Zr_{36}Ni_{64}$, which has been derived from interatomic distances by analyzing the measured partial structure factors. Furthermore, QENS measurements of liquid $Hf_{35}Ni_{65}$ prepared with ^{60}Ni, which has a vanishing incoherent scattering cross section, have demonstrated that self-diffusion of Hf is slowed down compared to the concentration weighted self-diffusion of Hf and Ni. This implies a dynamical decoupling between larger Hf and smaller Ni atoms, which can be related to a saturation effect of unequal atomic nearest-neighbor pairs, that was observed recently for Ni-rich compositions in Zr-Ni metallic melts. In order to establish a structure-dynamics relation, measured partial structure factors have been used as an input for mode-coupling theory (MCT) of the glass transition to calculate self-diffusion coefficients for the different atomic components. Remarkably, MCT can reproduce the increased activation energy for $Hf_{35}Ni_{65}$ as well as the dynamical decoupling between Hf and Ni atoms.

DOI: 10.1103/PhysRevB.96.054201

I. INTRODUCTION

The investigation of the structure-dynamics relation in metallic melts is essential to understand how the dynamical behavior of individual alloy components are controlled by structural differences on the atomic scale [1–8]. While the systematic investigation in multicomponent systems is complicated due to many different atomic species and, thus, numerous different atomic-pair interactions, binary metallic melts provide a unique opportunity to study dynamical and structural properties in detail by measuring the self-diffusion coefficients of individual alloy components as well as partial static structure factors [9,10]. Within the framework of the mode-coupling theory (MCT) of the glass transition, one can establish a structure-dynamics relation and thus predict transport properties, such as self-diffusion coefficients, using static partial structure factors as an input [11]. This approach has already been applied for $Zr_{64}Ni_{36}$ melts at a fixed temperature where MCT predicts equal diffusion coefficients of both Ni and Zr atoms [12]. This prediction has recently been confirmed through radiotracer measurements [13]. In order to investigate how the atomic dynamics of different alloy components are correlated with variations in the short-range order (SRO), it is necessary to compare MCT calculations with measured self-diffusion coefficients, thus underscoring the importance of experimentally determining the self-diffusion coefficient of both atomic species in a binary melt.

An important question that we will address here is whether different alloy components in the melt show the same dynamical behavior or exhibit a dynamical decoupling where the self-diffusion coefficient of one atomic species is different from that of the other [14]. Two different cases of dynamical decoupling in metallic melts have been reported. The first one shows a different temperature dependence for different atomic species close to the glass-transition temperature T_g below the critical temperature T_c of MCT as, for example, in the bulk metallic glass-former (BMG) $Pd_{43}Cu_{27}Ni_{10}P_{20}$ [15]. This "energetic decoupling" might be driven by strong changes in the activation energy of diffusion coefficients and cannot be explained by MCT since the temperature is below T_c. The second decoupling effect results from a similar temperature dependence for different atomic species, albeit with a different absolute value of the diffusion coefficient. In contrast to the first one, the latter effect can be explained by MCT and will be discussed in this paper concerning the correlation to structural features in the SRO for different alloy components.

Recently, the atomic dynamics of binary Zr-based glass-forming melts have been investigated using quasielastic neutron scattering (QENS) [16–19]. Substituting the late transition metals (Ni, Co, and Cu) yields a similar temperature dependence of the self-diffusion coefficients as well as a similar activation energy for self-diffusion in the different alloys. The difference in self-diffusion coefficients on the absolute scale between various compositions is less than a factor of 2 at the same temperature. However, in those studies it was only possible to measure the self-diffusion coefficient of the late transition metals (Ni, Co, and Cu) as Zr has a negligible incoherent scattering cross section ($\sigma_{Zr}^{inc} = 0.02$ barn) [20] and thus the self-diffusion coefficient of Zr cannot be determined in these alloy melts by using QENS.

Since our goal is to measure the self-diffusion coefficient of both atomic species in binary metallic melts and compare these results to MCT calculations, we substituted the early

*Benedikt.Nowak@dlr.de

transition-metal Zr by Hf, which has, in contrast to Zr, a non-negligible incoherent scattering cross section of $\sigma_{\mathrm{Hf}}^{\mathrm{inc}} = 2.6$ barn [20]. Pure Hf and Zr are chemically similar since they are in the same main group of the periodic table and have approximately the same atomic size [21]. For this reason, previous diffusion studies have employed Hf radiotracers as substitutes for Zr atoms in Zr-based BMGs [22]. In the case of Hf-Ni melts, this substitution allows us to investigate the self-diffusion coefficient of both alloy components also by QENS. For samples containing natural Ni ($\sigma_{\mathrm{Ni}}^{\mathrm{inc}} = 5.2$ barn), we measure a mean value of Ni and Hf self-diffusion. Furthermore, replacing natural Ni with ^{60}Ni allows us to measure only the Hf self-diffusion coefficient since ^{60}Ni has an incoherent scattering cross section of zero. Thus, we can study the relative dynamical behaviors of Hf and Ni and, if present, the differences between them, such as dynamical decoupling.

This paper aims to address the following questions:

(1) Are the SRO and the atomic dynamics of Hf-Ni and Zr-Ni melts similar or are there specific differences?

(2) Is it possible to identify structural properties that give rise to describe the observed dynamical behavior?

(3) Is the MCT able to predict correctly the atomic dynamics for different alloy components in Hf-Ni melts as previously for Zr-Ni only by using measured partial structure factors as an input?

II. EXPERIMENTAL DETAILS

An experimental challenge to performing neutron-scattering experiments on Hf-based melts is the large absorption cross section of Hf ($\sigma_{\mathrm{Hf}}^{\mathrm{abs}} \approx 295$ barn at $\lambda = 5.1$ Å) compared to that of Zr ($\sigma_{\mathrm{Zr}}^{\mathrm{abs}} \approx 0.5$ barn at $\lambda = 5.1$ Å) [20]. In order to obtain a high signal-to-background ratio from the strongly absorbing sample, we used the novel approach of combining neutron scattering with electrostatic levitation [18]. The high signal-to-background ratio can be explained by the absence of sample holders or crucibles in the vicinity of the sample, which allows us to measure even strongly absorbing systems with good data quality. To further reduce the impact of absorption, we have chosen both a small sample size of roughly 3 mm in diameter and a shorter incoming neutron wavelength for the QENS experiments, in contrast to the measurements on levitated Zr-Ni samples. Furthermore, we focused on the Ni-rich composition $Hf_{35}Ni_{65}$ since the absorption cross section of Ni ($\sigma_{\mathrm{Ni}}^{\mathrm{abs}} \approx 13$ barn at $\lambda = 5.1$ Å) [20] is much smaller compared to that of Hf.

For investigating the atomic dynamics, we performed QENS experiments at the chopper time-of-flight spectrometer TOFTOF [23,24] at the research neutron source Heinz-Meier-Leibniz (FRM-II). QENS probes the melt dynamics on a pico- to nanosecond time scale, which is too short to be affected by effects of macroscopic convective flow in the sample. Measurements were performed at 1470, 1525, 1600, and 1645 K for Hf_{35} $^{\mathrm{nat}}Ni_{65}$ and at 1470 and 1600 K for Hf_{35} $^{60}Ni_{65}$. For the measurements at 1470 K for Hf_{35} $^{\mathrm{nat}}Ni_{65}$ and at 1470 and 1600 K for Hf_{35} $^{60}Ni_{65}$, the employed wavelength was $\lambda = 5.1$ Å, and the chopper speed was 12000 rpm, resulting in an elastic instrumental energy resolution of roughly 100 μeV. The 2θ range of the detector from 7° to 140° gives access to a q range of 0.25–2.15 Å^{-1} at zero energy transfer. For the measurements at 1525, 1600, and 1645 K for Hf_{35} $^{\mathrm{nat}}Ni_{65}$, a different wavelength of $\lambda = 4.4$ Å was used with a chopper speed of 18 000 rpm. At this setting, the instrumental energy resolution remains unchanged, and the accessible q range at zero energy transfer was 0.25–2.55 Å^{-1}. The temperature of the melt was measured using a single-color pyrometer with an uncertainty of ±10 K. The temperature was calibrated at the known liquidus temperature ($T_{\mathrm{L}}^{\mathrm{Hf_{35}Ni_{65}}} = 1463$ K), assuming that the emissivity remains constant [25].

For data treatment a normalization to a vanadium standard, subtraction of background, and correction of self-absorption was performed. A detailed description of data processing can be found in Ref. [26]. Since coherent contributions from the static structure factor $S^{\mathrm{coh}}(q)$ are negligible at low q ($q < 1.4$ Å^{-1}), the dynamic signal is dominated by incoherent scattering and thus reflects the self-diffusion of atoms in the melt. Additionally, there is a dynamical restriction towards low-q values if the quasielastic broadening is below roughly 10% of the instrumental energy resolution and results in a minimum value for the full width at half maximum (FWHM) in the dynamic structure factor $S(q,\omega)$ of 10 μeV. From this, we calculate the lower limit for detectable relaxational dynamics to correspond to $q \approx 0.7$ Å^{-1} as the broadening of the QENS peak in $S(q,\omega)$ would be too small to be resolved at lower q values.

In the low-q range between 0.7 and 1.3 Å^{-1}, the self-diffusion coefficients can be determined from the intermediate scattering function $S(q,t)$, describing the density-density correlation of the atoms in the melt [26]. This function is described by an exponential decay,

$$S(q,t) = f_0 \exp[-t/\tau(q)], \tag{1}$$

where f_0 is the amplitude and $\tau(q)$ is the structural relaxation time. The obtained $\tau(q)$ follows a q^{-2} dependence, indicating diffusive motion from which the self-diffusion coefficient D can be derived according to

$$D = 1/[\tau(q)q^2], \tag{2}$$

in the hydrodynamic limit $q \to 0$ [27]. The self-diffusion coefficients also were determined by fitting $S(q,\omega)$ with a Lorentzian function. In the regime dominated by incoherent scattering, the FWHM Γ of the Lorentzian is related to the self-diffusion coefficient by the formula $D = \Gamma(q)/(2\hbar q^2)$ [28,29]. The presented results for self-diffusion coefficients in this paper represent mean values of both equivalent data analysis procedures, and the results obtained from both procedures are equal within the range of the measurement error.

The measured diffusion coefficient for Hf_{35} $^{\mathrm{nat}}Ni_{65}$ represents an average from the self-diffusion coefficients D_{Ni} and D_{Hf} where Ni contributions are dominant. With the incoherent scattering cross sections $\sigma_{\mathrm{Ni}}^{\mathrm{inc}} = 5.2$ and $\sigma_{\mathrm{Hf}}^{\mathrm{inc}} = 2.6$ barn and the corresponding concentrations c, the contribution of the Ni atoms is estimated by $(\sigma_{\mathrm{Ni}}^{\mathrm{inc}} c_{\mathrm{Ni}})/(\sigma_{\mathrm{Ni}}^{\mathrm{inc}} c_{\mathrm{Ni}} + \sigma_{\mathrm{Hf}}^{\mathrm{inc}} c_{\mathrm{Hf}}) \approx 80\%$ [20]. To measure the self-diffusion coefficient D_{Hf} independently, we use a sample prepared with ^{60}Ni without any incoherent contributions from Ni ($\sigma_{^{60}\mathrm{Ni}}^{\mathrm{inc}} = 0$ barn) [20]. As a result, it is possible to measure the weighted self-diffusion coefficient of Ni/Hf as well as the Hf self-diffusion coefficient.

Due to the high absorption of Hf and the low scattered intensity, each measurement has been performed for slightly more than 1 h in order to reduce the statistical error. For the measurements of $Hf_{35}{}^{60}Ni_{65}$ it was necessary to increase the measuring time to 5 h as the scattered intensity is reduced by a factor of 5 compared to the sample prepared with natural Ni. The loss of sample mass due to evaporation was determined to be smaller than 2% during this extended processing. By assuming that the evaporated material is mainly Ni [30], this results in a change in the alloy composition of roughly 1 at. %. Recently, it has been shown that for Zr-Cu and Zr-Ni melts the concentration dependence of self-diffusion coefficients is weak [16,31]. This leads to the conclusion that a change in the alloy composition of roughly 1 at. % in Hf-Ni melts has negligible impact on the atomic dynamics. This can be confirmed by the fact that the measured spectra remained unchanged during the complete measurement of a sample at a given temperature within the statistical error.

Neutron-diffraction measurements were performed at the high-intensity two-axis diffractometer D20 at the Institut Laue-Langevin (ILL) with a wavelength of $\lambda = 0.94$ Å. The combination of neutron diffraction and isotopic substitution provides the opportunity to determine partial static structure factors by measuring three total structure factors of $Hf_{35}Ni_{65}$, each representing a different scattering contrast. In this case, we substituted three Ni isotopes with three different coherent scattering lengths (^{60}Ni, ^{58}Ni, and natural Ni). The measured raw data were corrected by background subtraction and accounting for inelastic scattering, multiple scattering, and sample self-absorption [32]. The detector efficiency and geometrical effects were corrected using a vanadium measurement in the same geometry since vanadium is a nearly perfect incoherent scatterer resulting in a q-independent scattering signal. A detailed description of the data treatment is given in Ref. [32].

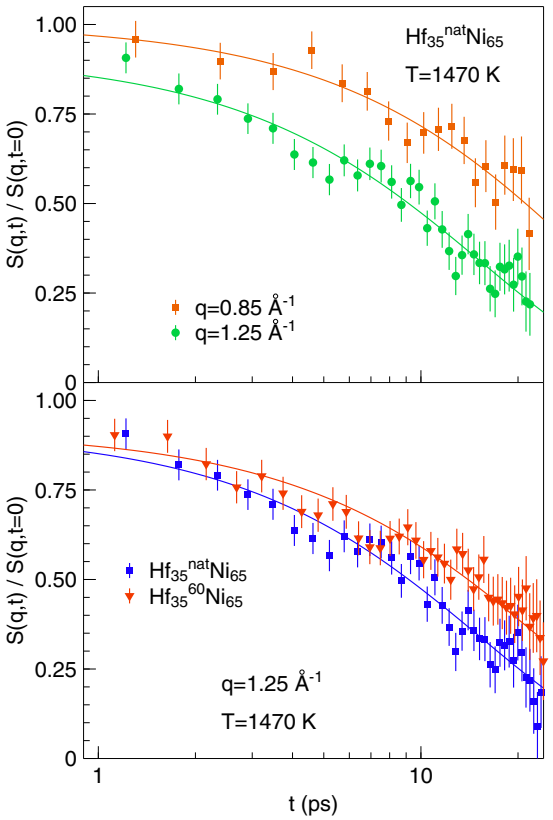

FIG. 1. Upper panel: Normalized intermediate scattering function $S(q,t)/S(q,t=0)$ for $Hf_{35}{}^{nat}Ni_{65}$ at 1470 K for two different momentum transfers at $q = 0.85$ and 1.25 Å^{-1}. The solid lines represent the exponential fit. Lower panel: $S(q,t)/S(q,t=0)$ for $Hf_{35}{}^{nat}Ni_{65}$ and $Hf_{35}{}^{60}Ni_{65}$ at 1470 K at $q = 1.25$ Å^{-1}.

III. RESULTS

A. Atomic dynamics

The normalized intermediate scattering function $S(q,t)/S(q,t=0)$ for $Hf_{35}{}^{nat}Ni_{65}$ at 1470 K is shown in the upper panel of Fig. 1 for two different q values. The lower panel displays $S(q,t)/S(q,t=0)$ for $Hf_{35}{}^{nat}Ni_{65}$ and $Hf_{35}{}^{60}Ni_{65}$ at 1470 K for $q = 1.25$ Å^{-1}.

The parameter $\tau(q)$ was determined by an exponential fit [see Eq. (1)] in the α-relaxation regime between 1 and 20 ps. The exponential function well describes the decay in the experimental data despite the increased scatter of the data compared to, e.g., Zr-Ni [31] or Zr-Cu [16] due to the large absorption cross section of Hf. In the fitting procedure, a stretched exponential $S(q,t) = f_0 \exp\{-[t/\tau(q)]^{\beta}\}$ with β as a free fit parameter also was tested; however, there was no significant effect on the fit quality and the resulting $\tau(q)$. For both fits the calculated self-diffusion coefficient is equal within the measurement error. Therefore, a single exponential function was used that has the advantage of a reduced number of free parameters. Deviations from the fit function around and below 1 ps are expected due to overlapping contributions of both fast atomic vibrations and self-diffusion. In the lower panel for $Hf_{35}{}^{60}Ni_{65}$ and $Hf_{35}{}^{nat}Ni_{65}$ at $q = 1.25$ Å^{-1} the amplitude f_0 of the exponential fit is roughly equal within the range of the measurement error, and deviations may arise from the normalization with $S(q,t=0)$ due to the extrapolation to $t = 0$.

To derive the self-diffusion coefficients, $1/\tau$ is plotted as a function of q^2 as shown in the upper panel of Fig. 2 for $Hf_{35}{}^{nat}Ni_{65}$ and $Hf_{35}{}^{60}Ni_{65}$ at 1470 K.

A linear q^2 dependence can be observed in the q range between $q = 0.7$ and 1.3 Å^{-1} where the incoherent contribution is dominant. In order to determine the self-diffusion coefficient D, a linear fit containing the origin (0,0) and values between $q^2 = 0.56$ and 1.69 Å^{-2} was carried out based on Eq. (2). This is corresponding to a constant $1/(\tau q^2)$ as a function of q^2 as shown in the lower panel of Fig. 2. The error of the self-diffusion coefficient is calculated from the standard deviation of $1/(\tau q^2)$ in the considered q range between $q^2 = 0.56$ and 1.69 Å^{-2}. At higher q values, coherent contributions become more and more dominant, and the values deviate from the linear regression (see the upper panel of Fig. 2). Due to the slow atomic dynamics below $q \approx 0.7$ Å^{-1} the relaxation time is much longer compared to the accessible time window up to 20 ps in Fig. 1. Consequently, we cannot accurately determine the relaxation time at these q values and, as discussed before, we only use data for $q > 0.7$ Å^{-1} to evaluate the self-diffusion coefficient.

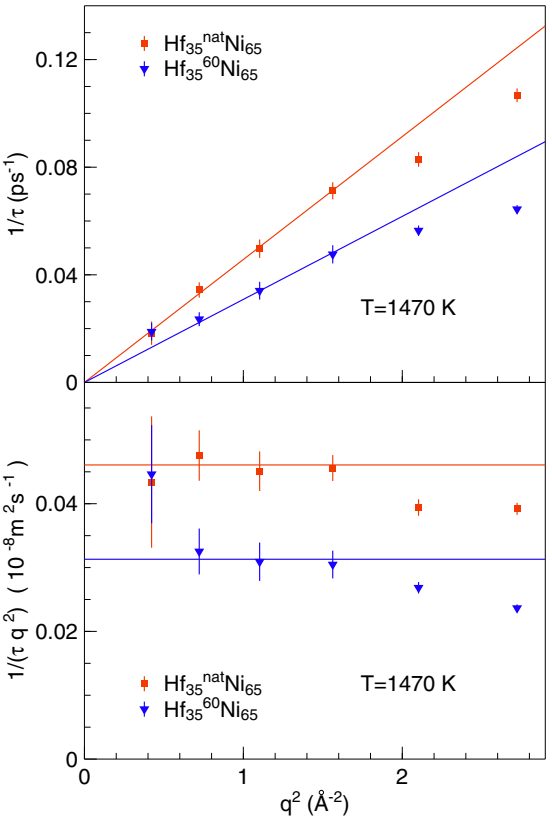

FIG. 2. Upper panel: Inverse structural relaxation time $1/\tau$ vs q^2 for $Hf_{35}{}^{nat}Ni_{65}$ and $Hf_{35}{}^{60}Ni_{65}$ at 1470 K. The solid lines represent the linear fit using (0,0) and values between $q^2 = 0.56$ and 1.69 Å^{-2} ($q = 0.7$ and 1.3 Å^{-1}). Lower panel: $\frac{1}{\tau(q)q^2}$ vs q^2 for $Hf_{35}{}^{nat}Ni_{65}$ and $Hf_{35}{}^{60}Ni_{65}$ at 1470 K.

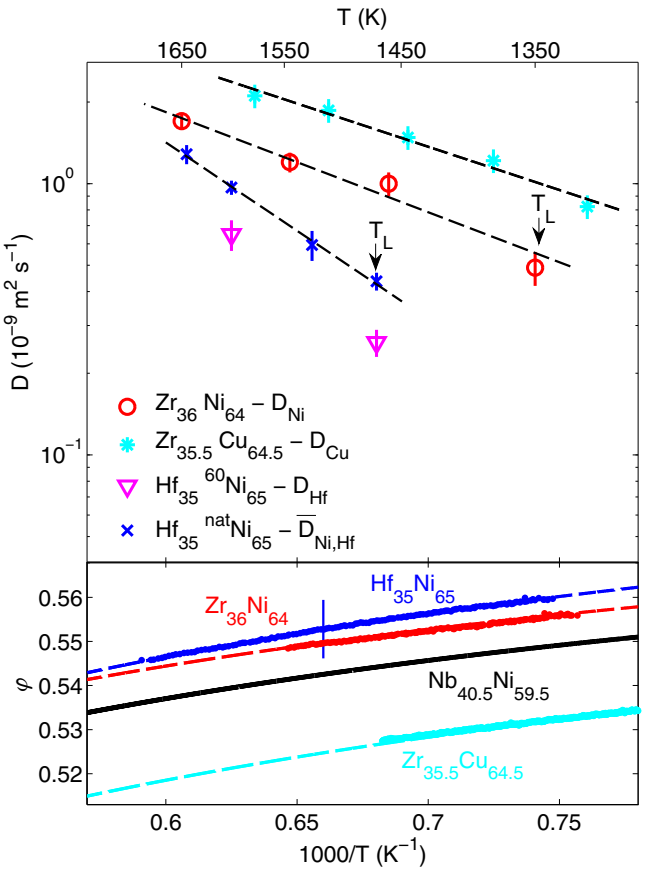

FIG. 3. Upper panel: Self-diffusion coefficients for $Zr_{36}Ni_{64}$ [31], $Zr_{35.5}Cu_{64.5}$ [16], $Hf_{35}{}^{nat}Ni_{65}$, and $Hf_{35}{}^{60}Ni_{65}$ measured by QENS. Lower panel: Packing fraction for $Zr_{36}Ni_{64}$, $Zr_{35.5}Cu_{64.5}$, $Hf_{35}Ni_{65}$, and $Nb_{40.5}Ni_{59.5}$ derived from macroscopic density measurements by using the covalent radii for the calculation [21] and the following parameters for the measured density of $Nb_{40.5}Ni_{59.5}$ [33]: $\rho(T) = 8.34–5.56 \times 10^{-4}(T - T_L)$ g cm^{-3} with the liquidus temperature of $T_L = 1448$ K. The vertical line represents the average experimental error.

The measured self-diffusion coefficients for $Hf_{35}{}^{nat}Ni_{65}$ (blue crosses), $Hf_{35}{}^{60}Ni_{65}$ (pink triangles), and $Zr_{36}Ni_{64}$ [31] (red circles) are shown in the upper panel of Fig. 3 and in Table I.

The Ni/Hf self-diffusion coefficient weighted by concentration and incoherent scattering cross sections measured for $Hf_{35}{}^{nat}Ni_{65}$ is about a factor of 1.5 (1600 K) or 1.7 (1470 K), respectively, larger compared to the Hf self-diffusion coefficient measured for $Hf_{35}{}^{60}Ni_{65}$. Since the Hf contribution (≈20%) reduces the mean Ni/Hf self-diffusion coefficient of the measurement with $Hf_{35}{}^{nat}Ni_{65}$, the pure Ni self-diffusion is thus faster by roughly a factor of 2 compared to the Hf self-diffusion. Such a dynamical decoupling between larger and smaller atoms has been observed recently in radiotracer measurements for the multicomponent BMG $Zr_{46.75}Ti_{8.25}Cu_{7.5}Ni_{10}Be_{27.5}$ [14] as well as for the binary glass-forming melt $Zr_{36}Ni_{64}$ [13].

The dashed lines in the upper panel of Fig. 3 represent an Arrhenius fit $D(T) = D_0 \exp[-E_A/(k_B T)]$ where D_0 is the diffusivity at infinite temperatures, k_B is the Boltzmann constant, and E_A is the activation energy. For $Hf_{35}{}^{nat}Ni_{65}$ we obtain an E_A for the mean Ni/Hf self-diffusion of (1.31 ± 0.06) eV. This value is nearly twice as large as for $Zr_{36}Ni_{64}$, which exhibits an E_A for Ni self-diffusion of (0.76 ± 0.11) eV [31].

In recent studies, differences in the dynamical behavior among various alloy systems have been related to different packing fractions where a denser atomic packing was used to explain a slower self-diffusion [16,34,35]. In this manner, the slowed-down diffusion for $Zr_{36}Ni_{64}$ compared to $Zr_{35.5}Cu_{64.5}$ (see the upper panel of Fig. 3) has been explained by the roughly 5% higher packing fraction of $Zr_{36}Ni_{64}$ (see the lower panel) [16]. When comparing the packing fractions of

TABLE I. Measured diffusion coefficient for $Hf_{35}{}^{nat}Ni_{65}$ and $Hf_{35}{}^{60}Ni_{65}$.

	T (K)	D (10^{-9} m^2 s^{-1})
$Hf_{35}{}^{nat}Ni_{65}$	1470 ± 5	0.44 ± 0.03
	1525 ± 5	0.59 ± 0.08
	1600 ± 5	0.97 ± 0.06
	1645 ± 5	1.28 ± 0.10
$Hf_{35}{}^{60}Ni_{65}$	1470 ± 5	0.26 ± 0.03
	1600 ± 5	0.65 ± 0.08

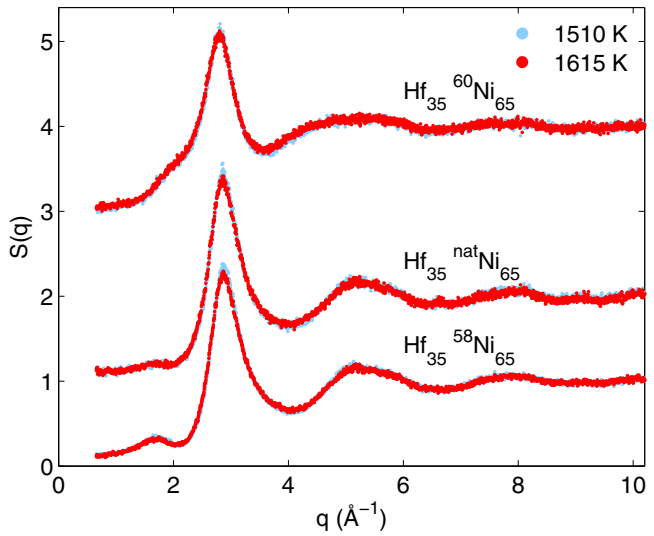

FIG. 4. Measured total static structure factors for $Hf_{35}{}^{60}Ni_{65}$, $Hf_{35}{}^{nat}Ni_{65}$, and $Hf_{35}{}^{58}Ni_{65}$ at 1510 and 1615 K. The curves are shifted along the vertical axis.

$Hf_{35}Ni_{65}$ and $Zr_{36}Ni_{64}$, the differences are rather small, and within the experimental error bars the packing fractions can be considered as equal. Hence differences in the packing fractions are not able to explain the significant differences in the atomic dynamics between Zr-Ni and Hf-Ni. In order to understand the structural reasons for the different dynamical behaviors on a microscopic level, we measured the partial structure factors for $Hf_{35}Ni_{65}$.

B. Short-range order

The measured total static structure factors for $Hf_{35}{}^{58}Ni_{65}$, $Hf_{35}{}^{nat}Ni_{65}$, and $Hf_{35}{}^{60}Ni_{65}$ at 1510 and 1615 K are shown in Fig. 4.

The results illustrate the weak temperature dependence for a temperature increase of 105 K. For comparison, in this temperature interval, the diffusion coefficients change by about a factor of 2.5. The measurement at lower temperatures shows slightly stronger oscillations, however the differences are very small. Partial static structure factors have been calculated from the total static structure factors within the Faber-Ziman and Bathia-Thornton formalisms, respectively [36,37] using formulas,

$$S(q)^{FZ} = \frac{c_A^2\overline{b_A}^2}{\overline{b^2}}S_{AA}(q) + \frac{c_B^2\overline{b_B}^2}{\overline{b^2}}S_{BB}(q) + \frac{2c_Ac_B\overline{b_Ab_B}}{\overline{b^2}}S_{AB}(q), \quad (3)$$

and

$$S(q)^{BT} = \frac{\overline{b}^2}{\overline{b^2}}S_{NN}(q) + \frac{c_Ac_B(\overline{b_A}-\overline{b_B})^2}{\overline{b^2}}S_{CC}(q) + \frac{2(\overline{b_A}-\overline{b_B})\overline{b}}{\overline{b^2}}S_{NC}(q), \quad (4)$$

TABLE II. Weightings of the partial structure factors in each of the measured total $S(q)$'s.

	$\frac{\overline{b}^2}{\overline{b^2}}$	$\frac{c_Ac_B(\overline{b_A}-\overline{b_B})^2}{\overline{b^2}}$	$\frac{2(\overline{b_A}-\overline{b_B})\overline{b}}{\overline{b^2}}$	$\frac{c_A^2\overline{b_A}^2}{\overline{b^2}}$	$\frac{c_B^2\overline{b_B}^2}{\overline{b^2}}$	$\frac{2c_Ac_B\overline{b_Ab_B}}{\overline{b^2}}$
$Hf_{35}{}^{58}Ni_{65}$	0.934	0.066	1.039	0.563	0.047	0.324
$Hf_{35}{}^{nat}Ni_{65}$	0.983	0.017	0.544	0.500	0.081	0.402
$Hf_{35}{}^{60}Ni_{65}$	0.789	0.211	−1.719	0.128	0.281	0.380

A = Ni, B = Hf.

with concentration c and coherent scattering length b of atom types A and B ($\overline{b} = c_A\overline{b_A} + c_B\overline{b_B}$ and $\overline{b^2} = c_A\overline{b_A^2} + c_B\overline{b_B^2}$). The weightings of the partial structure factors in each of the measured total $S(q)$'s are shown in Table II.

The results are shown in Fig. 5. The measured partial structure factors have been smoothed by using a slide average function since MCT requires a minimum standard of input data quality. The partial static structure factors for $Zr_{36}Ni_{64}$ at 1385 K are shown for comparison [38].

The Bathia-Thornton partial structure factors S_{NN} of $Hf_{35}Ni_{65}$ at 1510 K and $Zr_{36}Ni_{64}$ at 1385 K are roughly equal. It was not possible to measure the two alloys at the same

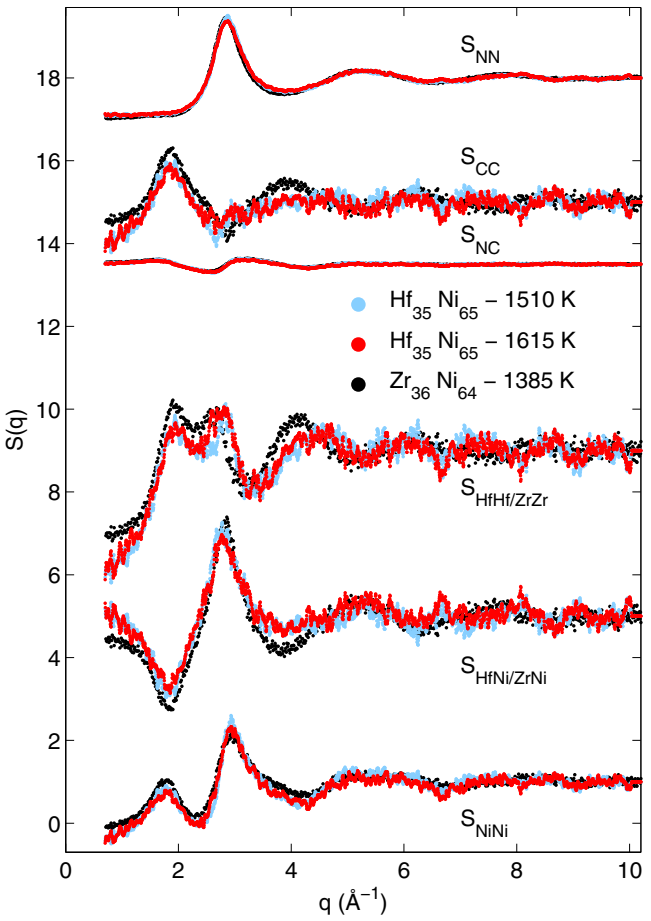

FIG. 5. Partial static structure factors calculated using the Faber-Ziman and Bathia-Thornton formalism for $Hf_{35}Ni_{65}$ at 1510 and 1615 K and $Zr_{36}Ni_{64}$ at 1385 K [36,37]. The curves are shifted along the vertical axis.

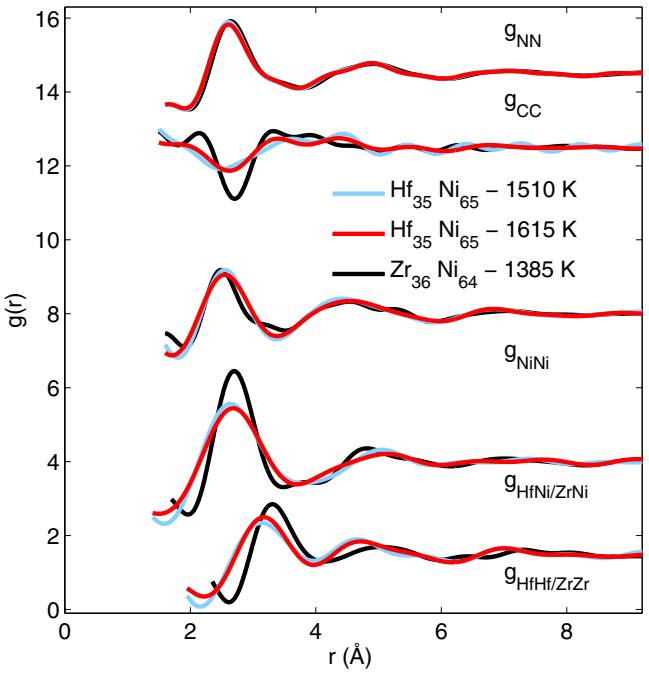

FIG. 6. Pair-correlation functions for $Hf_{35}Ni_{65}$ and $Zr_{36}Ni_{64}$ calculated using the Bathia-Thornton and Faber-Ziman formalisms. The curves are shifted along the vertical axis.

temperature due to the large difference in the liquidus temperature of T_L ($T_L^{Hf_{35}Ni_{65}} = 1463$ K [25] and $T_L^{Zr_{36}Ni_{64}} = 1343$ K [39]) and the limited undercoolability of the $Hf_{35}Ni_{65}$ melt. Nevertheless, considering the small differences in S_{NN} for $Hf_{35}Ni_{65}$ at 1510 and 1615 K, i.e., the slightly reduced amplitude of the oscillations caused by the temperature increase of 105 K, one might conclude that even at an equal temperature for $Hf_{35}Ni_{65}$ and $Zr_{36}Ni_{64}$ S_{NN} is similar, indicating a similar topological SRO. The Bathia-Thornton partial structure factor S_{CC}, describing the chemical SRO (CSRO), shows strong oscillations for both alloys, which implies a pronounced chemical order. The amplitude of the oscillations observed for $Hf_{35}Ni_{65}$ is slightly lower as compared with $Zr_{36}Ni_{64}$, particularly in the q range of the second oscillation around 3 to 4 $Å^{-1}$. The Bathia-Thornton partial static structure factor S_{NC}, which describes the correlation between number density and chemical composition, is almost identical for all three measurements. For a further analysis of the SRO, we have calculated the Faber-Ziman partial static structure factors, which describe the different contributions of each of the atomic pairs (Ni-Ni, Hf/Zr-Ni, and Hf-Hf/Zr-Zr) to the total static structure factor $S(q)$. Partial pair-correlation functions were determined through Fourier transformation of the partial static structure factors. Results for $Hf_{35}Ni_{65}$ and $Zr_{36}Ni_{64}$ are plotted in Fig. 6.

The pair-correlation function g_{NiNi} is almost identical for both alloys. The first maximum of g_{ZrNi} is sharper compared to g_{HfNi}, which implies a broader distribution of Hf-Ni nearest-neighbor distances in comparison to Zr-Ni distances. The fact that the first maxima of g_{ZrNi} and g_{HfNi} are larger than the first maxima of g_{NiNi} and g_{ZrZr} (g_{HfHf}), respectively, implies that heterogeneous nearest-neighbor pairs are preferred in both alloy melts. The same conclusion can also be drawn from the observation of the minima in the Bathia-Thornton pair-correlation function g_{CC} around 2.6 Å. Moreover, it is remarkable that the first and second peaks of g_{HfHf} are shifted to smaller interatomic distances compared to g_{ZrZr}. This fact cannot be explained by a temperature effect since the shift of the first peak positions of g_{HfHf} between 1510 and 1615 K is very small in comparison to the difference between g_{HfHf} and g_{ZrZr}.

For a more quantitative description, we have calculated coordination numbers and nearest-neighbor distances. The nearest-neighbor distances correspond to the positions of the first maxima in the pair-correlation functions. The coordination numbers have been determined by integrating the first peak in the radial distribution function between its first and second minima. The results are compiled in Tables III and IV together with those for $Zr_{36}Ni_{64}$ [38] and $Nb_{40.5}Ni_{59.5}$ [40]. The coordination numbers for $Hf_{35}Ni_{65}$ and $Zr_{36}Ni_{64}$ are equal within the error of the measurement, which underlines a similar topological SRO for both alloys. The SRO around larger Hf and Zr atoms, respectively, is considerably different compared to smaller Ni atoms since the partial coordination numbers for Hf ($Z_{HfHf} + Z_{NiHf} \approx 16$) and Zr ($Z_{ZrZr} + Z_{NiZr} \approx 17$), respectively, are larger in comparison to Ni ($Z_{NiNi} + Z_{xNi} \approx 12$). The most striking observations are smaller nearest-neighbor distances $d_{HfHf} = 3.15$ Å as well as smaller second nearest-neighbor distances $d_{HfHf,2} = 4.66$ Å (derived from the position of the second maximum in g_{HfHf}) at 1510 K compared to the distances of $d_{ZrZr} = 3.31$ and $d_{ZrZr,2} = 5.02$ Å. The smaller interatomic distance between Hf-Hf compared to Zr-Zr might be interpreted as a locally higher packing density of Hf atoms in $Hf_{35}Ni_{65}$ in comparison to Zr atoms in $Zr_{36}Ni_{64}$. This may affect the dynamical behavior leading to more sluggish diffusion in $Hf_{35}Ni_{65}$ and, thus, a higher activation energy.

Despite the slightly different stoichiometry of the alloy, we compare the results obtained for $Hf_{35}Ni_{65}$ and $Zr_{36}Ni_{64}$ with findings on the structure [40] and dynamics [41] for the binary metallic melt $Nb_{40.5}Ni_{59.5}$, which shows a roughly similar dynamical behavior compared to $Hf_{35}Ni_{65}$ (see Fig. 7).

TABLE III. Coordination numbers Z_{xy} ($x, y =$ Zr, Nb, Hf, and Ni) inferred from the partial pair-correlation functions. The average coordination number $\langle Z \rangle$ has been inferred from Faber-Ziman partial coordination numbers.

x-Ni	%Ni	T (K)	Z_{NN}	$\langle Z \rangle$	Z_{xx}	$Z_{x\mathrm{Ni}}$	$Z_{\mathrm{Ni}x}$	Z_{NiNi}	Reference
Hf-Ni	65	1510	13.3 ± 0.5	13.2 ± 0.5	5.3 ± 0.5	5.6 ± 0.5	10.4 ± 0.5	6.2 ± 0.5	This paper
	65	1615	13.1 ± 0.5	13.0 ± 0.5	5.5 ± 0.5	5.4 ± 0.5	10.1 ± 0.5	6.3 ± 0.5	This paper
Zr-Ni	64	1385	13.8 ± 0.5	13.8 ± 0.5	6.2 ± 0.5	5.9 ± 0.5	10.4 ± 0.5	6.3 ± 0.5	[38]
Nb-Ni	59.5	1495	14.3 ± 0.5	14.4 ± 0.5	6.4 ± 0.5	6.6 ± 0.5	9.6 ± 0.5	6.8 ± 0.5	[40]

$x =$ Hf,Zr, or Nb.

TABLE IV. Nearest-neighbor distances d_{xy} (x, y = Zr, Nb, Hf, and Ni) inferred from the partial pair-correlation functions.

x-Ni	%Ni	T (K)	d_{NN} (Å)	d_{xx} (Å)	$d_{x\mathrm{Ni}}$ (Å)	d_{NiNi} (Å)	$d_{xx,2}$ (Å)	Reference
Hf-Ni	65	1510	2.62 ± 0.02	3.15 ± 0.02	2.65 ± 0.02	2.56 ± 0.02	4.65 ± 0.10	This paper
	65	1615	2.62 ± 0.02	3.18 ± 0.02	2.66 ± 0.02	2.56 ± 0.02	4.71 ± 0.10	This paper
Zr-Ni	64	1385	2.63 ± 0.02	3.31 ± 0.02	2.70 ± 0.02	2.51 ± 0.02	5.02 ± 0.10	[38]
Nb-Ni	59.5	1495	2.61 ± 0.02	3.00 ± 0.02	2.64 ± 0.02	2.51 ± 0.02	4.63 ± 0.10	[40]

x = Hf, Zr, or Nb.

In addition, partial static structure factors for $Nb_{40.5}Ni_{59.5}$ have been measured previously [40], and we are thus able to analyze structural features in detail. Remarkably, the Ni self-diffusion coefficient of $Zr_{36}Ni_{64}$ is greater as compared to that in $Nb_{40.5}Ni_{59.5}$ (see Fig. 7), although the packing fraction of $Zr_{36}Ni_{64}$ is slightly higher in comparison to $Nb_{40.5}Ni_{59.5}$ ($\approx$1%) (see the lower panel of Fig. 3) [33]. This finding is obviously at odds with the assumption that a higher atomic packing fraction generally results in slowed-down diffusion. Therefore, the sluggish dynamics in $Nb_{40.5}Ni_{59.5}$ cannot be explained by overall average packing fraction arguments, and the SRO of individual atomic species need to be analyzed. For this reason, we studied the previous features concerning sluggish diffusion due to locally higher packing of the larger atomic species for $Nb_{40.5}Ni_{59.5}$ as well. In order to account for the smaller atomic radius of the early transition-metal Nb in $Nb_{40.5}Ni_{59.5}$ compared to Zr and Hf [21], we analyze the difference between the measured interatomic distance d_{xx} in the alloy melt (see Table IV) and twice of the Goldschmidt radii [42] $2r_{\mathrm{G}}^{x}$ of the pure elements (x = Zr, Hf, and Nb). The smaller the difference, the denser the local packing of the atomic species x in the alloy melt compared to the monoatomic melt. We obtain

$$\Delta d_{\mathrm{ZrZr}} = d_{\mathrm{ZrZr}} - 2r_{\mathrm{G}}^{\mathrm{Zr}} = 0.11 \text{ Å},$$
$$\Delta d_{\mathrm{NbNb}} = d_{\mathrm{NbNb}} - 2r_{\mathrm{G}}^{\mathrm{Nb}} = 0.06 \text{ Å},$$
$$\Delta d_{\mathrm{HfHf}} = d_{\mathrm{HfHf}} - 2r_{\mathrm{G}}^{\mathrm{Hf}} = -0.01 \text{ Å},$$
$$\Delta d_{\mathrm{ZrNi}} = d_{\mathrm{ZrNi}} - \left(r_{\mathrm{G}}^{\mathrm{Zr}} + r_{\mathrm{G}}^{\mathrm{Ni}}\right) = -0.15 \text{ Å},$$
$$\Delta d_{\mathrm{NbNi}} = d_{\mathrm{NbNi}} - \left(r_{\mathrm{G}}^{\mathrm{Nb}} + r_{\mathrm{G}}^{\mathrm{Ni}}\right) = -0.08 \text{ Å},$$
$$\Delta d_{\mathrm{HfNi}} = d_{\mathrm{HfNi}} - \left(r_{\mathrm{G}}^{\mathrm{Hf}} + r_{\mathrm{G}}^{\mathrm{Ni}}\right) = -0.18 \text{ Å}.$$

The differences of the heterogeneous interatomic distances Δd_{ZrNi}, Δd_{NbNi}, and Δd_{HfNi} are smaller than zero, which implies an affinity of unequal nearest neighbors in all three alloy melts. This finding can be explained by strong interactions between unequal atomic components, which lead to shorter interatomic distances in the alloy melts compared to interatomic distances in the monoatomic systems. Since the difference Δd_{ZrZr} for $Zr_{36}Ni_{64}$ is slightly larger in comparison to Δd_{HfHf}, this finding indicates a less-dense packing for Zr atoms in $Zr_{36}Ni_{64}$ compared to Hf atoms in $Hf_{35}Ni_{65}$. The difference Δd_{NbNb} for $Nb_{40.5}Ni_{59.5}$ is also slightly smaller in comparison to Δd_{ZrZr}, and thus Nb atoms are denser packed compared to Zr atoms, even though the value for Δd_{NbNb} is in between Δd_{ZrZr} and Δd_{HfHf}. Here one also should bear in mind the slightly different stoichiometry of $Nb_{40.5}Ni_{59.5}$. The reduced differences Δd_{HfHf} and Δd_{NbNb} compared to Δd_{ZrZr} are the most striking features between the alloy melts. This suggests that the sluggish diffusion in $Hf_{35}Ni_{65}$ and $Nb_{40.5}Ni_{59.5}$ might arise from the locally higher packing density of the larger atomic species, identified by the smaller differences Δd_{NbNb} and Δd_{HfHf}. On the other hand, the average packing fractions of the melts derived from density measurements are roughly equal, and the deviation is smaller than 2% among $Zr_{36}Ni_{64}$, $Hf_{35}Ni_{65}$, and $Nb_{40.5}Ni_{59.5}$ [33]. Thus, the average packing fractions cannot be correlated with the differences of the self-diffusion coefficients in these melts. Consequently, a local effect in the SRO, such as the locally higher packing densities of Hf and Nb atoms, might be the reason for the observed variations in the atomic dynamics when substituting the early transition-metal component.

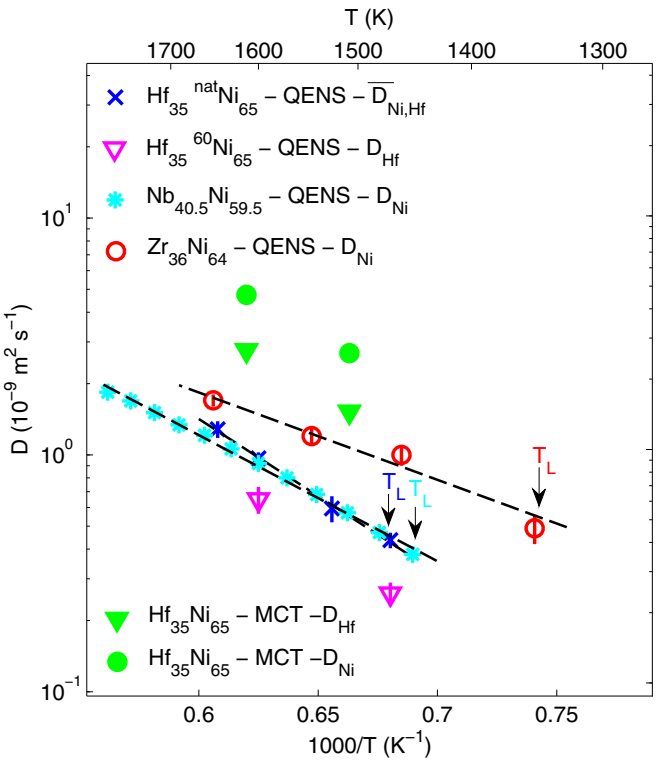

FIG. 7. Self-diffusion coefficients for $Zr_{36}Ni_{64}$ [31], $Nb_{40.5}Ni_{59.5}$ [41], $Hf_{35}{}^{\mathrm{nat}}Ni_{65}$, and $Hf_{35}{}^{60}Ni_{65}$ measured by QENS (open symbols). Calculated self-diffusion coefficients of Ni and Hf by MCT for $Hf_{35}Ni_{65}$ from measured partial static structure factors (green full symbols).

C. Mode-coupling theory and structure-dynamics relation

In order to analyze the structure-dynamics relation in more detail, the partial static structure factors of $Hf_{35}Ni_{65}$ at 1510

and 1615 K shown in Fig. 5 were used as an input for MCT to calculate transport coefficients. The MCT results for calculated Hf and Ni self-diffusion coefficients are shown in Fig. 7 as full symbols.

The deviation of MCT from the QENS results on the absolute scale is as a result of the fact that the temperature enters only as an indirect parameter in MCT calculations. This has been discussed in Ref. [38] in detail for $Zr_{50}Ni_{50}$. Remarkably, MCT and QENS results for $Hf_{35}Ni_{65}$ in Fig. 7 show a similar temperature dependence and thus a roughly identical activation energy for self-diffusion coefficients. Despite the very small changes in the partial static structure factors caused by a temperature increase of about 105 K, MCT can accurately reproduce the activation energy of the diffusion coefficients. The remarkably good agreement of activation energies between QENS and MCT results has also been observed for $Zr_{50}Ni_{50}$ by a temperature increase over 220 K [38]. Moreover, the dynamical decoupling observed here in the QENS results, i.e., Ni atoms diffuse faster than Hf atoms, can be reproduced by the MCT calculations as well (Fig. 7). The decoupling found in the MCT results ($D_{Ni}/D_{Hf} = 1.8$) is close to the experimental QENS results, which reveal a decoupling of roughly a factor of 2. Although static partial structure factors only provide space- and time-averaged structural information of the alloy melt, they are sufficient to reveal the dynamical decoupling of the diffusion coefficients as well as the activation energy for self-diffusion when serving as an input for MCT.

We also have calculated the Nb and Ni self-diffusion coefficient of $Nb_{40.5}Ni_{59.5}$ by MCT using measured partial static structure factors as an input [40]. As illustrated by MCT results in the upper panel of Fig. 8, a dynamical decoupling also is predicted for $Nb_{40.5}Ni_{59.5}$ ($D_{Ni}/D_{Nb} = 1.4$). However, the ratio of the Ni and Nb self-diffusion is smaller compared to $Hf_{35}Ni_{65}$ ($D_{Ni}/D_{Hf} = 1.8$) and $Zr_{36}Ni_{64}$ ($D_{Ni}/D_{Zr} = 1.8$).

In order to investigate the impact of the different atomic sizes on dynamical behavior without any contributions of the CSRO, we utilized a hard-sphere (HS) model approximation where chemical interactions between atoms are neglected and the packing density is the only input parameter. In doing so, we consider the case of $Nb_{40.5}Ni_{59.5}$ where the atomic radius of Nb ($r_{cov} = 1.34$ Å) is slightly smaller compared to Zr ($r_{cov} = 1.45$ Å) and Hf ($r_{cov} = 1.44$ Å), thus allowing us to investigate the impact of the atomic size of the early transition metal [21]. With a $r_{cov} = 1.15$ Å for Ni the size ratio amounts to 1.17 for $Nb_{40.5}Ni_{59.5}$ and to 1.26 for $Zr_{36}Ni_{64}$ (see the black crosses in the upper panel of Fig. 8). Results out of the HS approximation indicate a ratio between the self-diffusion coefficients of larger and smaller atoms of ≈1.6 for the HS mixture with the corresponding size ratio of $Nb_{40.5}Ni_{59.5}$ and of ≈2.0 for the HS mixture with the corresponding size ratio of $Zr_{36}Ni_{64}$. Since the ratio for $Nb_{40.5}Ni_{59.5}$ is smaller in MCT calculations ($D_{Ni}/D_{Nb} = 1.4$) as well as in the HS model (≈1.6), one might assume that the smaller atomic size of Nb in contrast to the larger atomic size of Zr may lead to the reduced ratio of dynamical decoupling. However, the ratio is influenced by a different CSRO and other influencing factors, which unfortunately prevents a conclusive explanation.

For Zr-Ni melts it has been argued that the decoupling effect may be explained by an excess of less-strongly interacting Ni atoms, which can diffuse more freely in a background

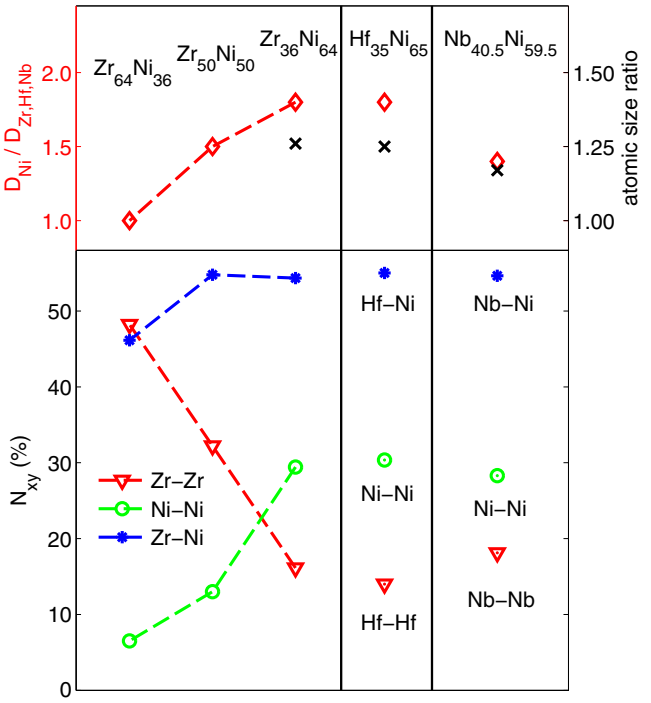

FIG. 8. Upper panel: Ratio of the self-diffusion coefficients for $Zr_{36}Ni_{64}$, $Zr_{50}Ni_{50}$, $Zr_{64}Ni_{36}$, $Hf_{35}Ni_{65}$, and $Nb_{40.5}Ni_{59.5}$ calculated by MCT using measured partial static structure factors are plotted as red diamonds [38]. The black crosses are the ratio of the atomic sizes (r^x_{cov}/r^{Ni}_{cov}; x = Zr, Hf, and Nb). Lower panel: Fractions of atomic nearest-neighbor pairs as a function of Ni concentration for $Zr_{36}Ni_{64}$, $Zr_{50}Ni_{50}$, $Zr_{64}Ni_{36}$, $Hf_{35}Ni_{65}$, and $Nb_{40.5}Ni_{59.5}$ [38,40].

of saturated unequal atomic nearest-neighbor pairs [38]. For this purpose, the different fractions of atomic nearest-neighbor pairs N_{xy} have been determined by using the the coordination numbers Z_{xy}, the atomic concentrations c_x ($x, y =$ Ni, Zr, Nb, and Hf), and the following equations:

$$N_{xx} = \frac{c_x Z_{xx}}{\langle Z \rangle}, \qquad N_{xy} = \frac{c_x Z_{yx} + c_y Z_{xy}}{\langle Z \rangle}. \tag{5}$$

The results are compiled in Table V and illustrated in Fig. 8.

As shown in the figure, in $Zr_{64}Ni_{36}$ the fraction of Ni-Ni nearest-neighbor pairs N_{NiNi}, which represents the amount of excess less-strongly interacting Ni atoms, is only around 7%. With an increasing amount of Ni in the Zr-Ni melt,

TABLE V. Fraction of different atomic nearest-neighbor pairs N_{xy} ($x, y =$ Zr, Hf, Nb, and Ni).

x-Ni	%Ni	T (K)	N_{xx}	N_{xNi}	N_{NiNi}	Reference
Zr-Ni	36	1375	48%	46%	7%	[38]
	50	1445	32%	55%	13%	[38]
	50	1665	32%	55%	14%	[38]
	64	1385	16%	54%	30%	[38]
Hf-Ni	65	1510	14%	55%	30%	This paper
	65	1615	15%	53%	31%	This paper
Nb-Ni	59.5	1495	18%	55%	28%	Calc. from data of Ref. [40]

x = Zr, Hf, or Nb.

N_{NiNi} increases, and diffusion becomes decoupled because of an increased amount of excess Ni atoms with higher mobility, which can diffuse more freely in a background of saturated heterogeneous nearest-neighbor pairs [38]. In the Ni-rich alloys $Zr_{36}Ni_{64}$, $Hf_{35}Ni_{65}$, and $Nb_{40.5}Ni_{59.5}$, the fraction of Ni-Ni nearest-neighbor pairs N_{NiNi} is roughly equal. Remarkably, the fraction of heterogeneous nearest-neighbor pairs is also equal ($N_{\mathrm{ZrNi}} \approx N_{\mathrm{HfNi}} \approx N_{\mathrm{NbNi}} \approx 55\%$), despite the differences in the atomic radii of the early transition metals between Nb and Zr/Hf. The saturation effect seems to be the origin for the experimentally as well as theoretically observed dynamical decoupling of diffusion coefficients of different alloy components in the Ni-rich binary metallic melts, which have been studied in the framework of this paper.

IV. SUMMARY

In conclusion, we have investigated the microscopic structure-dynamics relation in Ni-rich binary metallic melts with different early transition metals with a focus on the temperature dependence as well as the relative dynamical behavior between different alloy components. The three questions that have been emphasized at the end of the Introduction will be answered accurately below.

Our results indicate that the sluggish diffusion and the increased activation energy for self-diffusion coefficients observed for $Hf_{35}Ni_{65}$ and $Nb_{40.5}Ni_{59.5}$ in comparison to $Zr_{36}Ni_{64}$ can be related to a locally higher packing density of Hf and Nb atoms in $Hf_{35}Ni_{65}$ and $Nb_{40.5}Ni_{59.5}$ compared to the Zr atoms in $Zr_{36}Ni_{64}$. Although the overall average packing fraction of the melts is roughly equal, these distinct differences concerning the local atomic packing of the larger atomic species have been identified by analyzing partial pair-correlation functions. As a generic effect in the Ni-rich binary melts we have studied, we find a dynamical decoupling of the diffusivities of the atomic species, and that this decoupling is driven by a saturation of chemical interactions of Ni. Although the investigated melts generally show pronounced chemical ordering that in turn suggests atomic diffusivities to be coupled strongly, beyond a certain Ni concentration, the diffusivity of Ni is dominated by "unbound," and thus faster, Ni atoms. This effect was first observed in Zr-Ni melts [38], and our present investigation shows that it applies to Hf-Ni and, as predicted by MCT, to Nb-Ni as well. This suggests that the effect of dynamical decoupling caused by a saturation effect is not restricted to special atomic interactions or a specific type of SRO and thus might be extended to other metallic melts with preferred heterogeneous nearest-neighbor pairs, such as Zr-Co [19] or Al-Ni [43]. Moreover, the saturation effect may explain the dynamical decoupling observed in multicomponent metallic melts, e.g., $Zr_{46.75}Ti_{8.25}Cu_{7.5}Ni_{10}Be_{27.5}$ [14] and maybe even in nonmetallic systems.

Structural parameters, such as nearest-neighbor distances and fractions of different atomic nearest-neighbor pairs, derived from experimentally measured partial structure factors, characterize the SRO and are able to explain the observed dynamical effects for the three investigated alloys. In addition, the experimentally observed dynamical behavior could be reproduced by MCT using measured partial structure factors as an input to calculate transport coefficients. The MCT and QENS results show a remarkably good agreement concerning activation energy and dynamical decoupling. This highlights that the time- and space-averaged structural information provided by measured partial structure factors determines the temperature dependency of self-diffusion coefficients as well as the relative dynamical behavior between different alloy components.

ACKNOWLEDGMENTS

We would like to thank S. Zimmermann, E. Ritter, C. Reinerth, and S. Szabó for their help during the experiments at ILL and FRM-II. W. Lohstroh and H. Meier are gratefully acknowledged for their technical support at the TOFTOF spectrometer.

[1] Y. Q. Cheng, H. W. Sheng, and E. Ma, Phys. Rev. B **78**, 014207 (2008).
[2] S. Hao, C. Wang, M. Kramer, and K. Ho, J. Appl. Phys. **107**, 053511 (2010).
[3] Y. Lü, H. Cheng, and M. Chen, J. Chem. Phys. **136**, 214505 (2012).
[4] N. Jakse and A. Pasturel, Appl. Phys. Lett. **105**, 131905 (2014).
[5] A. Jaiswal, T. Egami, and Y. Zhang, Phys. Rev. B **91**, 134204 (2015).
[6] L. Xiong, K. Chen, F. Ke, H. Lou, G. Yue, B. Shen, F. Dong, S. Wang, L. Chen, C. Wang *et al.*, Acta Mater. **92**, 109 (2015).
[7] N. Jakse and A. Pasturel, J. Chem. Phys. **144**, 244502 (2016).
[8] A. E. Lagogianni, J. Krausser, Z. Evenson, K. Samwer, and A. Zaccone, J. Stat. Mech.: Theor. Exp. (2016) 084001.
[9] M. Maret, T. Pomme, A. Pasturel, and P. Chieux, Phys. Rev. B **42**, 1598 (1990).
[10] S. Gruner, J. Marczinke, L. Hennet, W. Hoyer, and G. Cuello, J. Phys.: Condens. Matter **21**, 385403 (2009).
[11] W. Götze, J. Phys.: Condens. Matter **11**, A1 (1999).
[12] T. Voigtmann, A. Meyer, D. Holland-Moritz, S. Stüber, T. Hansen, and T. Unruh, Europhys. Lett. **82**, 66001 (2008).
[13] S. W. Basuki, F. Yang, E. Gill, K. Rätzke, A. Meyer, and F. Faupel, Phys. Rev. B **95**, 024301 (2017).
[14] S. W. Basuki, A. Bartsch, F. Yang, K. Rätzke, A. Meyer, and F. Faupel, Phys. Rev. Lett. **113**, 165901 (2014).
[15] A. Bartsch, K. Rätzke, A. Meyer, and F. Faupel, Phys. Rev. Lett. **104**, 195901 (2010).
[16] F. Yang, D. Holland-Moritz, J. Gegner, P. Heintzmann, F. Kargl, C. C. Yuan, G. G. Simeoni, and A. Meyer, Europhys. Lett. **107**, 46001 (2014).
[17] F. Faupel, W. Frank, M.-P. Macht, H. Mehrer, V. Naundorf, K. Rätzke, H. R. Schober, S. K. Sharma, and H. Teichler, Rev. Mod. Phys. **75**, 237 (2003).
[18] T. Kordel, D. Holland-Moritz, F. Yang, J. Peters, T. Unruh, T. Hansen, and A. Meyer, Phys. Rev. B **83**, 104205 (2011).

[19] M. D. Ruiz-Martín, D. Holland-Moritz, F. Yang, C. C. Yuan, G. G. Simeoni, T. Hansen, U. Rütt, O. Gutowski, J. Bednarcik, and A. Meyer (to be published) (2017).
[20] V. F. Sears, Neutron News **3**, 26 (1992).
[21] L. Pauling, J. Am. Chem. Soc. **69**, 542 (1947).
[22] T. Zumkley, M. P. Macht, V. Naundorf, J. Rüsing, and G. Frohberg, J. Metastable Nanocryst. Mater. **8**, 135 (2000).
[23] T. Unruh, J. Neuhaus, and W. Petry, Nucl. Instrum. Methods Phys. Res., Sect. A **580**, 1414 (2007).
[24] Heinz Maier-Leibnitz Zentrum *et al.*, J. Large-Scale Research Facilities **1**, A15 (2015).
[25] P. Nash and A. Nash, Bull. Alloy Phase Diagrams **4**, 250 (1983).
[26] F. Yang, T. Kordel, D. Holland-Moritz, T. Unruh, and A. Meyer, J. Phys.: Condens. Matter **23**, 254207 (2011).
[27] J. P. Boon and S. Yip, *Molecular Hydrodynamics* (McGraw-Hill, New York, 1980).
[28] J. Hansen and I. McDonald, *Theory of Simple Liquids* (Academic, London, 1986).
[29] S. Szabó and Z. Evenson, Appl. Phys. Lett. **110**, 161903 (2017).
[30] C. Alcock, V. Itkin, and M. Horrigan, Can. Metall. Q **23**, 309 (1984).
[31] D. Holland-Moritz, S. Stüber, H. Hartmann, T. Unruh, and A. Meyer, J. Phys.: Conf. Ser. **144**, 012119 (2009).
[32] D. Holland-Moritz, T. Schenk, P. Convert, T. Hansen, and D. M. Herlach, Meas. Sci. Technol. **16**, 372 (2005).
[33] S. Mukherjee, Z. Zhou, W. L. Johnson, and W.-K. Rhim, J. Non-Cryst. Solids **337**, 21 (2004).
[34] D. Holland-Moritz, S. Stüber, H. Hartmann, T. Unruh, T. Hansen, and A. Meyer, Phys. Rev. B **79**, 064204 (2009).
[35] S. Stüber, D. Holland-Moritz, T. Unruh, and A. Meyer, Phys. Rev. B **81**, 024204 (2010).
[36] T. E. Faber and J. M. Ziman, Philos. Mag. **11**, 153 (1965).
[37] A. Bhatia and D. Thornton, Phys. Rev. B **2**, 3004 (1970).
[38] B. Nowak, D. Holland-Moritz, F. Yang, T. Voigtmann, T. Kordel, T. C. Hansen, and A. Meyer, Phys. Rev. Materials **1**, 025603 (2017).
[39] P. Nash and C. Jayanth, Bull. Alloy Phase Diagrams **5**, 144 (1984).
[40] D. Holland-Moritz, F. Yang, J. Gegner, T. Hansen, M. D. Ruiz-Martín, and A. Meyer, J. Appl. Phys. **115**, 203509 (2014).
[41] S. M. Chathoth, B. Damaschke, M. M. Koza, and K. Samwer, Phys. Rev. Lett. **101**, 037801 (2008).
[42] C. J. Smithells, *Metals Reference Book*, edited by E. A. Brandes (Butterworths, London, 1983).
[43] P. Kuhn, J. Horbach, F. Kargl, A. Meyer, and T. Voigtmann, Phys. Rev. B **90**, 024309 (2014).